Microstructure Evolution and Properties of Laser Cladding CoCrFeNiTiAl$_x$ High-Entropy Alloy Coatings

Yiku Xu [1,*], Zhiyuan Li [1], Jianru Liu [1], Yongnan Chen [1,*], Fengying Zhang [1], Lei Wu [1], Jianmin Hao [1] and Lin Liu [2]

[1] School of Material Science and Engineering, Chang'an University, Xi'an 710064, China; 2018231020@chd.edu.cn (Z.L.); ljr568094730@163.com (J.L.); zhangfengying@chd.edu.cn (F.Z.); wulei@chd.edu.cn (L.W.); h-jianmin@126.com (J.H.)

[2] State Key Laboratory of Solidification and Processing, Northwestern Polytechnical University, Xi'an 710072, China; linliu@nwpu.edu.cn

* Correspondence: xuyiku23@chd.edu.cn (Y.X.); chenyongnan@chd.edu.cn (Y.C.); Tel.: +86-29-82334590 (Y.X.); +86-29-82337343 (Y.C.)

check for updates

Abstract: High-entropy alloy (HEA) coatings of CoCrFeNiTiAl$_x$ (x = 0, 0.5, 1, 1.5, 2) were prepared on the surface of AISI1045 steel by laser cladding. The effects of the Al content on the microstructure, composition, phase constitution, and wear and corrosion resistance of the coatings were investigated. The results showed that when increasing the Al element content from 0 to 0.5, the phase constitution of the CoCrFeNiTiAl$_x$ coating changed from a single Face-centered cubic (FCC) phase to Body-centered cubic 1 (BCC1) and Body-centered cubic 2 (BCC2) phases, with a small amount of Laves phase, which obviously improved the friction and corrosion resistance of the coating. With further enhancing of the Al content, the amount of BCC1 phase increased, while the BCC2 phase and the Laves phase decreased. The CoCrFeNiTiAl$_2$ HEA coating transformed into a single BCC1 phase, with retrogressive wear and corrosion resistance. It was found that the Al$_{0.5}$ alloy coating exhibits excellent wear resistance, high hardness, and corrosion resistance in a 3.5 wt.% NaCl solution. Furthermore, the effect of the Al content on the microstructure, phase, and the relating properties of the CoCrFeNiTiAl$_x$ HEA coatings is also discussed.

Keywords: high-entropy alloy coating; laser cladding; microstructure; wear resistance; corrosion resistance

1. Introduction

Traditional alloy design considers that the presence of multiple elements in an alloy results in the formation of intermetallic compounds (IMCs), which is detrimental to alloy performance. However, Ye JW proposed the concept of high-entropy alloys (HEAs) in 2004 [1]. An HEA is composed of five or more constituent elements, as per the mole ratio or the nearly mole ratio. The design principle prioritizes the high entropy effect, which inhibits the formation of brittle IMCs with complex crystal structures, instead forming a simple type of alloy solid solution phase [2]. The formation of high-entropy solid solution alloys must satisfy certain conditions. Zhang et al. used three main parameters ($8.5 \geq \delta \geq 0$, 7 kJ/mol $\geq \Delta H_{mix} \geq -22$ kJ/mol, and 19.5 J/(K·mol) $\geq \Delta S_{mix} \geq 11$ J/(K·mol)) to characterize the common behavior of constituent elements in HEAs [3]. They are atomic size difference δ, mixing enthalpy ΔH_{mix}, and mixing entropy ΔS_{mix}, and their respective expressions are:

$$\delta = 100 \sqrt{\sum_{i=1}^{n} c_i (1 - r_i / \bar{r})^2} \tag{1}$$

$$\Delta H_{\text{mix}} = \sum_{i=1, i \neq j}^{n} \Omega_{ij} c_i c_j \tag{2}$$

$$\Delta S_{\text{mix}} = -R \sum_{i=1}^{n} c_i \ln c_i \tag{3}$$

A lot of research has reported HEAs with excellent hardness, strength, and corrosion and wear resistances [2–6], a typical example being that of the CoCrFeNi HEA system. For example, CoCrFeNiMn HEA has higher yield strength (518 MPa) and ultimate tensile strength (660 MPa), and the maximum yield strength of $Al_{0.7}CoCrFeNi$ HEA is 1022 MPa [7,8]. Due to their excellent performance, HEA coatings are also prepared to protect the substrates in different ways. The commonly used processes for preparing alloy coatings are plasma spraying and high-velocity oxygen fuel (HVOF) spraying [9–11]. However, recently, the process of preparing alloy coating by laser cladding has become common [12,13]. Laser cladding is characterized by high energy density, fast heating and cooling rates, a lower heat effect on the base material, and a low dilution rate. The coating microstructure is of lower uniform density and micro-defects and forms excellent metallurgical bonds with the matrix material independent of size [14], Matilainen et al. prepared AlCoCrFeNi HEAs by laser additive manufacturing, and it is found that the solidification rate is a very important factor that determines the existence and distribution of phases in AlCoCrFeNi HEA, fast solidification substantially increases the preference for the BCC phase with a corresponding substantial increase in hardness. It should be noted that this is also related to some parameters such as specific powder, laser beam speed, and power density [15].

As reported, the key factor affecting the alloying behavior and properties of HEA is its elemental composition design. Al and Ti have been investigated in many articles involving HEA due to the larger atomic radius and characteristics of these elements having greater impact on the structural property characteristic of HEAs [12,16–19]. Liu et al. prepared an $AlCoCrFeNiTi_x$ (x = 0, 0.2, 0.4, 0.6, 0.8, 1.0) coating on AISI1045 steel by laser cladding technology and studied the corrosion behavior of the HEA coating in a 3.5 wt.% NaCl solution. The results proved that the introduction of Ti improves the corrosion resistance of the coating [12]. Zhang et al. used laser cladding technology to prepare a FeCoCrAlNi HEA coating on 304 stainless steel, which exhibited good corrosion resistance and microhardness [13]. However, Kao et al. studied the corrosion resistance of $Al_xCoCrFeNi$ HEA and found that the self-corrosion potential (E_{corr}) and self-corrosion current (I_{corr}) were independent of the Al content [20], which conflicts with previous studies. Thus, it is important to study the effect of additive elements for better understanding the HEA systems.

In this work, $CoCrFeNiTiAl_x$ HEA coatings were prepared using laser cladding technology. The performance of the as-prepared HEA coatings and the effect of Al content on the microstructure, phase constitution, and wear and corrosion resistance of the coatings were investigated.

2. Materials and Methods

AISI1045 steel with dimensions of 80 by 60 by 10 mm^3 was selected as the substrate. It was cleaned with absolute ethanol as the pretreatment in order to guarantee high matrix-coating bonds. Commercial Co, Cr, Fe, Ni, Ti, and Al powders with purities higher than 99.9 wt.% were used as raw materials. The particle sizes of the powders were determined to be 75–100 μm. The powders were weighed according to the nominal composition of $CoCrFeNiTiAl_x$ (x = 0, 0.5, 1, 1.5, 2 in molar ratio) using a precise electronic balance, the quality of each component is shown in Table 1. To ensure uniform mixing of the HEA powder during cladding, the ball-to-powder ratio (mass ratio) was set to 2:1 and mixed at a speed of 300 r/min in a QE-04 planetary ball mill for an hour. Then, a single lap

multi-layer of laser cladding feeding powder was carried out under an argon atmosphere with an LSF-SI6000A equipment (BLT, Xian, China), as shown in Figure 1. The specific process parameters are listed in Table 2.

Table 1. The mass of elements of CoCrFeNiTiAl$_x$ high entropy alloy coatings (g).

Element	Co	Cr	Fe	Ni	Ti	Al
CoCrFeNiTi	23.56	20.80	22.40	23.48	19.16	0
CoCrFeNiTiAl$_{0.5}$	23.56	20.80	22.40	23.48	19.16	5.40
CoCrFeNiTiAl$_1$	23.56	20.80	22.40	23.48	19.16	10.80
CoCrFeNiTiAl$_{1.5}$	23.56	20.80	22.40	23.48	19.16	16.20
CoCrFeNiTiAl$_2$	23.56	20.80	22.40	23.48	19.16	21.60
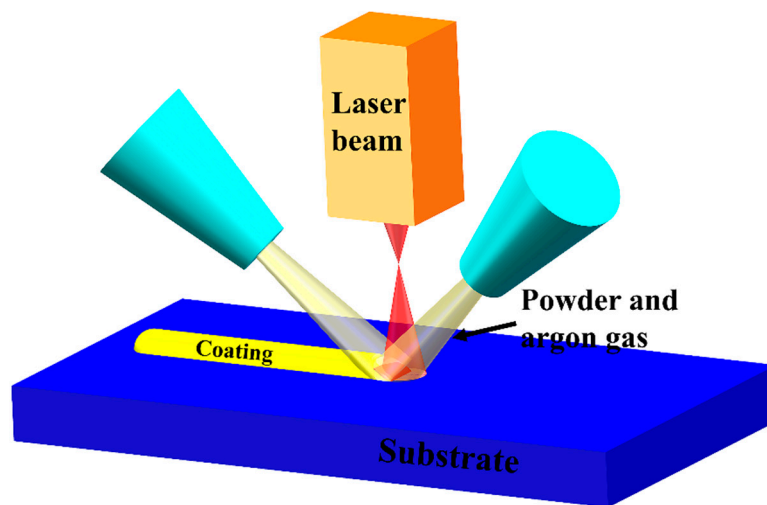
Figure 1. Schematic diagram of the laser cladding.

Table 2. Process parameters of laser cladding.

Parameters	Data
Laser power	2100 W
Scan speed	9 mm/s
Laser beam diameter	5 mm
Single layer thickness	0.2 mm
Layers	30
Mass of feed powder	8 g/min
Cladding area	60×30 mm^2

After laser cladding, the prepared coating material was sectioned into samples measuring 8 by 8 by 4 mm^3 using a wire electric discharge machine. The samples were ground and polished using a polishing machine. The microstructure of the HEA coatings was observed by the Hitachi S-4800 cold field emission scanning electron microscope (SEM, Hitachi, Tokyo, Japan) applying an energy dispersive spectrometer (EDS, Hitachi, Tokyo, Japan) to determine the element composition and the field emission transmission electron microscope (TEM, FEI, Hillsboro, OR, USA) Talos F200X. The phase constitution was determined using X-ray diffraction (Bruker D8 Advance model), using Cu–Kα radiation scanning from 30° to 90° at a scanning rate of 8° min^{-1}, the volume fraction of the phases was calculated by using Image-Pro Plus software (Image-Pro Plus 6.0). The microhardness of the sample was measured using a microhardness tester (HV-1000A, Shanghai Optical Instrument Factory, Shanghai, China) with a load value of 200 g and a holding time of 10 s. The average value of seven different points was taken as the hardness of the sample. Before the friction and abrasion test, the mass of each sample was weighed by an electronic balance. At room temperature and air relative humidity of

25%–30%, the friction and wear behavior of the coating was evaluated using a pin-disk wear machine (MMQ-02G, KASON, Jinan, China). The GCr15 bearing steel ball with a diameter of 6 mm was selected as the abrasive material, and the prepared sample was fixed on the disk of the worktable. The GCr15 bearing steel ball started the friction and wear test at the center of the sample. The process parameters are as follows: The load is 10 N, the speed is 100 r/min, and the time is 15 min. Considering that the initial stage of the friction and wear test did not reach a stable state, we took the value in the interval of 301 s–900 s to calculate the average friction coefficient. After the friction coefficient measurement was completed, the mass of each sample after the friction test was re-weighed. The corrosion behavior of the HEA coating in a 3.5 wt.% NaCl solution was studied by using an electrochemical workstation. The sample to be tested was used as a working electrode (WE), with the platinum plate electrode used as a counter electrode (CE), and a saturated calomel electrode (Hg/Hg$_2$Cl$_2$ saturated KCl) used as a reference electrode (RE). The potential scanning speed was 2 mV/s during the test, at a scanning range of approximately −1.5 to 0.5 V. The corrosion current density (I_{coor}) and self-corrosion potential (E_{coor}) were obtained by fitting the test results using the CorShow software (CorShow software 1.1.16).

3. Results and Discussion

3.1. Phase Constitution

Figure 2 shows the XRD diffraction patterns of the as-prepared laser cladding CoCrFeNiTiAl$_x$ HEA coatings with different Al contents. The Al$_0$ coating was composed of a single FCC solid solution phase. When increasing the molar ratio of Al (x = 0.5–1.5), the phase constitution of the coatings change from a single FCC phase to two BCC (BCC1 and BCC2) phases, and a small amount of Laves phase peaks can also be found. As can be seen with the increased Al content, the intensity of the diffraction peak of the BCC2 phase and the Laves phase begin to weaken, and simultaneously, the BCC1 phase peak increases. The Al$_2$ alloy coating transforms to a single phase with the BCC1 crystal structure. Using JADE software analysis, the BCC1 and BCC2 phases were identified as the Al–Ni phase and the Fe–Cr phase, and the Laves phase was identified as FeTi type, respectively.
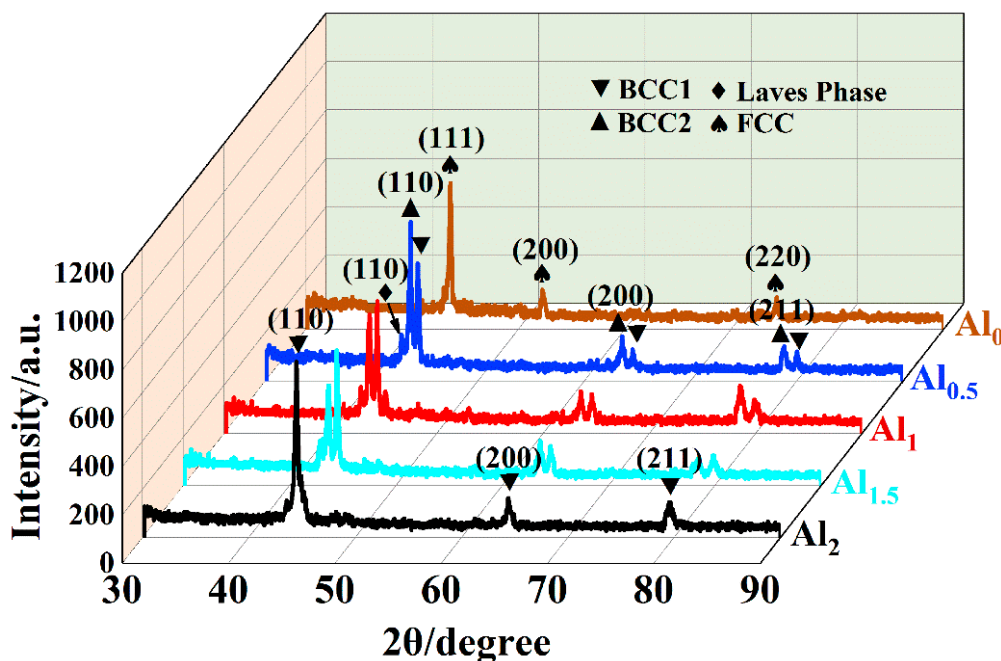

Figure 2. XRD diffraction patterns of the CoCrFeNiTiAl$_x$ (x = 0, 0.5, 1.0, 1.5, 2.0) coatings.

3.2. Microstructure Evolution

The microstructures of the CoCrFeNiTiAl$_x$ high-entropy alloy coatings are shown in Figure 3. The Al$_0$ coating in Figure 3a has a uniform single-phase structure with tiny voids, which is consistent with the XRD results. The laser cladding technology is characterized by rapid heating/cooling, which results in poor diffusion during the solidification process that prevents a small amount of gas from escaping when the molten pool solidifies, generating a small number of voids. The Al$_{0.5}$ coating shows a typical dendritic crystal, consisting of the dendritic region (DR) and interdendritic region (ID). With the increase of Al content, the number of dendrites gradually increases and the distance between dendrites becomes smaller. This is attributed to the introduction of Al with a relatively larger atomic radius, which leads to grain refinement. When the Al content increases to two, the alloy coating exhibits a uniform BCC1 phase structure. Compared to Al$_{0.5}$ in Figure 3a, the Al$_2$ coating shows more defects, such as the voids indicated by the arrows. Figure 3 proves that the Al content significantly influences the microstructure evolution of the CoCrFeNiTiAl$_x$ high-entropy alloy coatings.
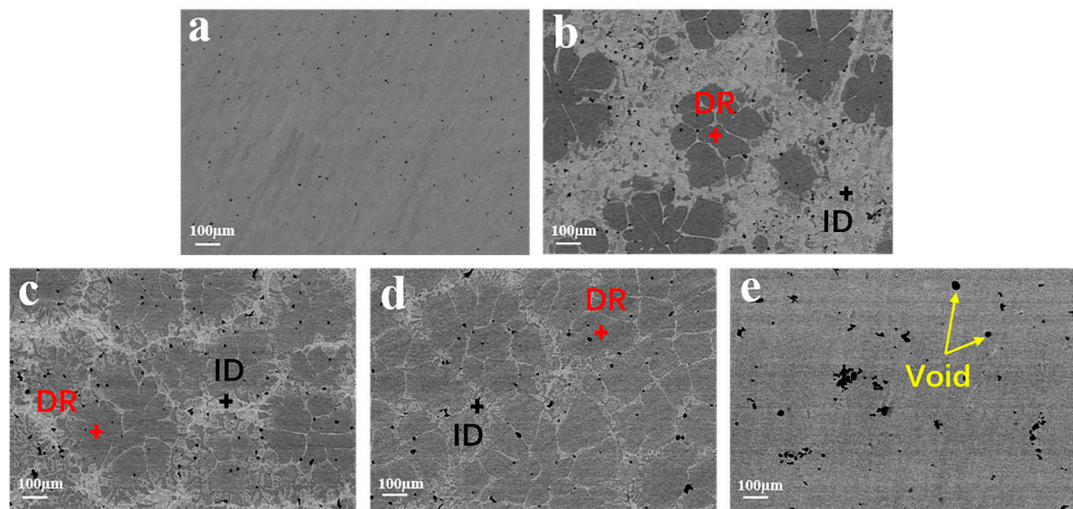

Figure 3. Scanning electron microscopy (SEM) micrographs of the CoCrFeNiTiAl$_x$ high-entropy alloy coatings: (**a**) Al$_0$ coating; (**b**) Al$_{0.5}$ coating; (**c**) Al$_1$ coating; (**d**) Al$_{1.5}$ coating; and (**e**) Al$_2$ coating. DR, dendritic region; ID, interdendritic region.

Figure 4a illustrates the morphology of a cross-section of the Al$_{0.5}$ coating. It can be seen that three zones comprise the cross-section, including the substrate, the heat-affected zone (HAZ), and the HEA coating (HEAC). The dilution rate of the coating can be calculated by Equation (4):

$$\eta = \frac{h}{H + h} \tag{4}$$

where η is the dilution rate, h is the substrate penetration, and H is the cladding layer width, coating dilution rate is 32.93%, the combination of the coating and substrate is metallurgical and continuous. Due to the dilution effect of the Fe element in the matrix, the content of each alloy element in the composition transition region significantly deviates from the nominal composition proved by the EDS line scan result. This dilution phenomenon generally affects the whole HAZ zone of the coating. As the distance increases from the substrate to the HEAC, the content of each element gradually approaches the nominal composition.
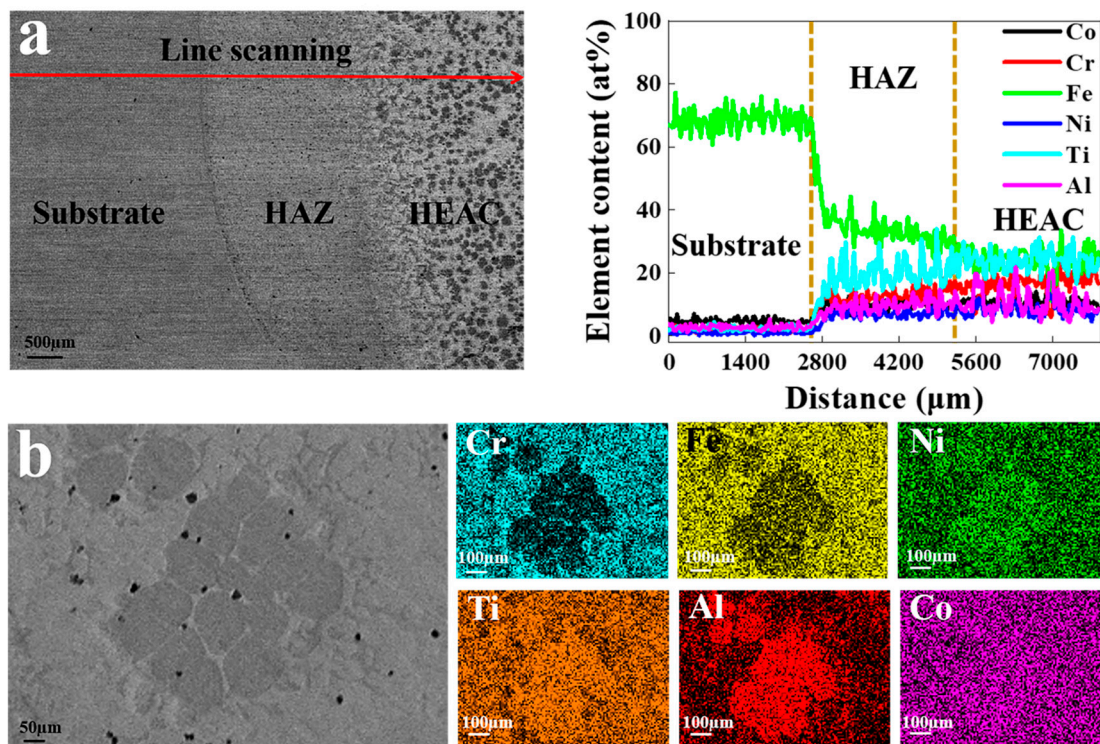
Figure 4. SEM of $Al_{0.5}$ high-entropy alloy coating: (**a**) cross-sectional morphology and selected area line scan of $Al_{0.5}$ high-entropy alloy coating and (**b**) elemental distribution maps of $Al_{0.5}$ high-entropy alloy coating. HAZ, heat-affected zone; HEAC, high-entropy alloy coating.

Elemental distribution maps of $Al_{0.5}$ HEA coating are illustrated in Figure 4b. It can be found that the DR is rich in Ni and Al elements, while the IR is rich in Fe and Cr elements. It has been reported that among multi-element metal elements, the more negative the mixing enthalpy, the greater the affinity between the two atoms, the more positive the mixing enthalpy, and the smaller the affinity [2,3,21]. According to the molar mixing enthalpy among the six elements shown in Table 3, the mixing enthalpy of Fe and Cr with the other five elements presents as the most positive, which signifies relatively small affinity. Consequently, when solidified, Fe and Cr elements are more easily repelled to the interdendritic region.

Table 3. Molar mixing enthalpy (ΔH_{mix} KJ·mol^{-1}) of binary alloys [3,21].

Element	Co	Cr	Fe	Ni	Ti	Al
Co	-	−4	−1	0	−28	−19
Cr	−4	-	−1	−7	−1	−10
Fe	−1	−1	-	−2	−17	−11
Ni	0	−7	−2	-	−35	−22
Ti	−28	−1	−17	−35	-	−30
Al	−19	−10	−11	−22	−30	-

3.3. Microhardness

The results of the microhardness test of the CoCrFeNiTiAl$_x$ HEA coatings are shown in Figure 5. The hardness distribution curves are divided into three parts in a step shape—the HEA coatings, the HAZ, and the substrate. The thickness of the coating is ~3.5 mm, compared with 2.5 mm of the HAZ. From the HEA coatings to the substrate, the hardness distribution shows a downward trend, and the decreasing interval is concentrated in the heat-affected zone. The $Al_{0.5}$ coating shows the highest hardness value of about 880 HV, which is 6.5 times as much as the substrate.

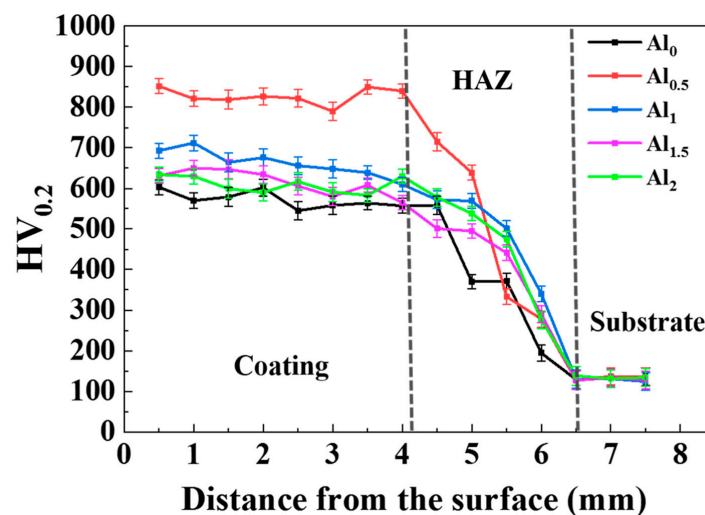**Figure 5.** The microhardness distribution curve of the CoCrFeNiTiAl$_x$ high-entropy alloy coatings.

3.4. Friction and Wear

The curves of the friction coefficients versus the sliding time acquired from the substrate and the CoCrFeNiTiAl$_x$ HEA coatings against the steel ball are shown in Figure 6a. All of the curves consist of a running-in stage initially, which is a process of removing the surface roughness and flattening the uneven surface with relatively small contact areas between the worn surface and the counterpart of the steel ball. After the rough initial surface becomes smooth, the wear enters a stable stage, exhibiting a stable friction coefficient. The average friction coefficient of the substrate is the largest, which is 0.54, and the Al$_0$ coating is also at a high level with an average friction coefficient of 0.42. It is obvious that, along with the addition of Al, the friction coefficient decreases sharply. The Al$_{0.5}$ HEA coating exhibits the smallest friction coefficient of about 0.28, compared with the Al$_1$, Al$_{1.5}$, and Al$_2$ coatings of about 0.31, 0.33, and 0.35, respectively.

The surface morphology of the coatings and substrate after wear are shown in Figure 6b. As can be seen, the substrate has the widest and deepest wear track, indicating its poor resistance to wear. Yet many furrows formed in the worn surface of the Al$_0$ coating, which may be due to the coating and abrasive ball being slightly adhered in the early stages of wear. The generated abrasive debris, the coating, and the abrasive material formed the three-body wear, indicating the abrasive wear mechanism of the Al$_0$ coating. The wear result of the Al$_{0.5}$ coating shows no furrows existing on the wear surface, and only slight adhesive wear occurred. With increasing Al content, the wear of the Al$_1$ and Al$_{1.5}$ coatings becomes more serious. The number of furrows and the depth increase, and the wear mechanism changes to micro-abrasive wear. In comparison, the wear morphology of the Al$_2$ coating emerges as obvious spalling, thus the wear mechanism of the Al$_2$ coating can be deduced to be micro-fracture (flake) wear.

The wear mass loss of the CoCrFeNiTiAl$_x$ high-entropy alloy coating and the substrate is also presented in Figure 6c. The wear amount of the Al$_0$ coating is 4.4 mg, and that of the Al$_{0.5}$ coating suddenly drops to 2.9 mg, reaching its minimum value. As the Al content increases, the wear amount of the Al$_1$, Al$_{1.5}$, and Al$_2$ coatings become 3.7 mg, 4.0 mg, and 4.2 mg, respectively. However, the wear of the five HEA coatings is still significantly lower than that of the substrate (19.7 mg). The Archard wear equation is an equation derived from a simplified model of abrasive wear, and although it does not take into account factors such as work hardening and frictional heat, it links the wear rate with the engineering variables and mechanical properties of the material. The expression of the Archard wear equation is [22]

$$\frac{W_v}{S} = K\frac{F}{H} \tag{5}$$

where W_v is the volume wear, S is the sliding distance, F is the normal load, H is the hardness of the wear material, and K is the wear coefficient. According to the previous microhardness tests, the microhardness descends in the order of $Al_{0.5}$, Al_1, $Al_{1.5}$, Al_2, and A_{10}, AISI1045 steel. The relationship between hardness and the amount of wear is inverse: The higher the hardness, the lower the wear. The experimental results are consistent with Archard's theoretical equations. Under the same wear condition, the wear rate of the as-prepared coatings is proportional to the friction coefficient and inversely proportional to the hardness.
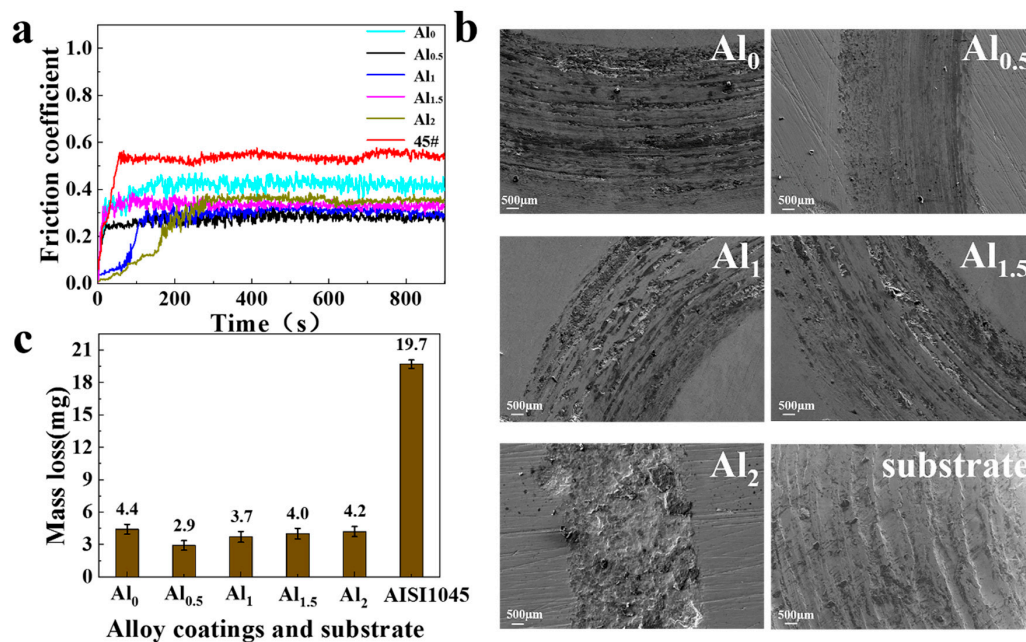

Figure 6. (**a**) variation of the friction coefficients versus test time for the CoCrFeNiTiAl$_x$ high-entropy alloy coatings and substrate; (**b**) SEM patterns after wearing of the CoCrFeNiTiAl$_x$ high-entropy alloy coatings and substrate; and (**c**) sass loss of the CoCrFeNiTiAl$_x$ high-entropy alloy coatings and substrate.

3.5. Corrosion Resistance

The potential dynamic polarization curve of the CoCrFeNiTiAl$_x$ HEA coatings and substrate in a 3.5 wt.% NaCl solution is shown in Figure 7. The corrosion dynamics parameters obtained using the Tafel epitaxy are shown in Table 4. The self-corrosion potential of the substrate is −0.9701 V, which is lower than the self-corrosion potential of the coating, and the self-corrosion current density is the largest, reaching 4.71×10^{-5} A·cm^{-2}. When increasing the Al content from 0 to 2, the corrosion resistance of the CoCrFeNiTiAl$_x$ HEA coating gradually increases, and then decreases. The $Al_{0.5}$ coating shows the best corrosion resistance; the maximum self-corrosion potential is −0.5766 V, and the minimum self-corrosion current density is 9.13×10^{-7} A·cm^{-2}.

Table 4. Corrosion dynamics parameters for the CoCrFeNiTiAl$_x$ HEA coatings and the AISI1045 steel.

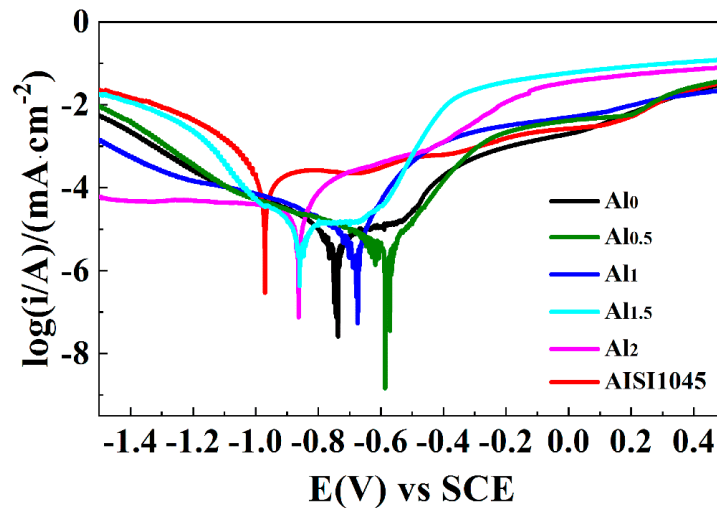| Sample No.	b_a (mV)	b_c (mV)	E_{corr}/V	I_{corr}/(A·cm^{-2})
Al_0	227.05	149.37	−0.7382	5.60×10^{-6}
$Al_{0.5}$	140.14	78.60	−0.5766	9.13×10^{-7}
Al_1	90.25	102.11	−0.6791	5.43×10^{-6}
$Al_{1.5}$	157.32	146.30	−0.8591	8.03×10^{-6}
Al_2	48.80	58.86	−0.8802	9.14×10^{-6}
AISI1045	40.97	46.244	−0.9701	4.71×10^{-5}

Figure 7. Tafel polarization curves of the CoCrFeNiTiAl$_x$ high-entropy alloy coatings and the AISI1045 steel.

3.6. Discussion

It has been reported that the addition of Al can change the phase constitution and the microstructure of HEA [16–18]. Figure 8a displays the TEM bright-field image of the Al$_{0.5}$ coating. The EDS mapping in Figure 8d proves that the white area is rich in Fe and Cr elements, while the gray area is rich in Al and Ni elements. Being consistent with the XRD result, the gray and white areas are confirmed to be the BCC1 and BCC2 phases, BCC1 is an ordered phase, respectively. According to our XRD and SEM results, it can be concluded that compared with the XRD data of Al$_{0.5}$ coating, the BCC1 phase diffraction peaks of Al$_{1.0}$ and Al$_{1.5}$ shifted slightly to the left, the BCC2 phase diffraction peaks did not change, and the lattice constant of BCC1 phase of Al$_{0.5}$ coating was 0.2881 nm and BCC2 phase lattice constant is 0.29 nm. The Laves phase is a transition region from BCC2 to BCC phase, and its lattice constant is 0.2912 nm, which can be identified as FeTi type. Figure 8c clearly shows that there are some nano-precipitates between the BCC1 and BCC2 phases, with a diameter of about 15–20 nm, and these nano-precipitates rarely occur in the Laves phase. Based on the kinetic theory, due to the relatively slow long-distance diffusion of phase separation in high-entropy alloys with multiple major elements, when laser cladding, the cooling rate is very fast, substitutional diffusion of the elements becomes difficult, resulting in the generation of nano-precipitates. Figure 8e displays the line scan results and Table 5 lists the composition analysis. It is obvious that the elements of the Laves phase are more uniformly distributed compared to the enriched BCC1 and BCC2 phases, which proves that the Laves phase is a transition region from the BCC2 phase to the BCC1 phase. Simultaneously, this phenomenon was proved by XRD, seen in Figure 2, where the BCC1 phase peak shifts to the left as the Al element increases. The scan angles corresponding to the main diffraction peaks of the BCC1 phase of the Al$_{0.5}$, Al$_{1.0}$, and Al$_{1.5}$ coatings were approximately 43.513°, 43.525°, and 43.548°, respectively. The left shift of the BCC1 phase peak can be explained by the Bragg diffraction law, which is expressed as:

$$2dsin\theta = n\lambda(n = 1, 2\ldots) \tag{6}$$

where *d* is the interplanar distance, θ is the angle between the incident X-ray and the corresponding crystal plane, *n* is the diffraction order, and λ is the wavelength of the X-ray. It can be seen from Equation (6) that as the interplanar spacing increases, the diffraction angle decreases; because the atomic radius of the Al atom is large, the introduction of the Al atom will lead to an increase in the lattice parameter of the BCC1 phase, and when Al is added to CoCrFeNiTi alloys with FCC structure, the elements solid-solve with each other to form a higher lattice distortion energy, which results in a high energy metastable state of the alloy system. The structural changes of high-entropy alloys caused

by Al addition can be explained by the atomic packing efficiency of FCC and BCC [23]. As the FCC structure has the highest density of atomic arrangements (74%), in order to release the increasing lattice distortion energy, the structure tends to transform into a BCC structure with a lower atomic density (68%), forming a stable structure with lower energy; this trend becomes more apparent as the Al content increases [24]. In addition, the FCC phase in HEAs transforming to the BCC phase through the addition of Al element has also been proven by many research works [25].
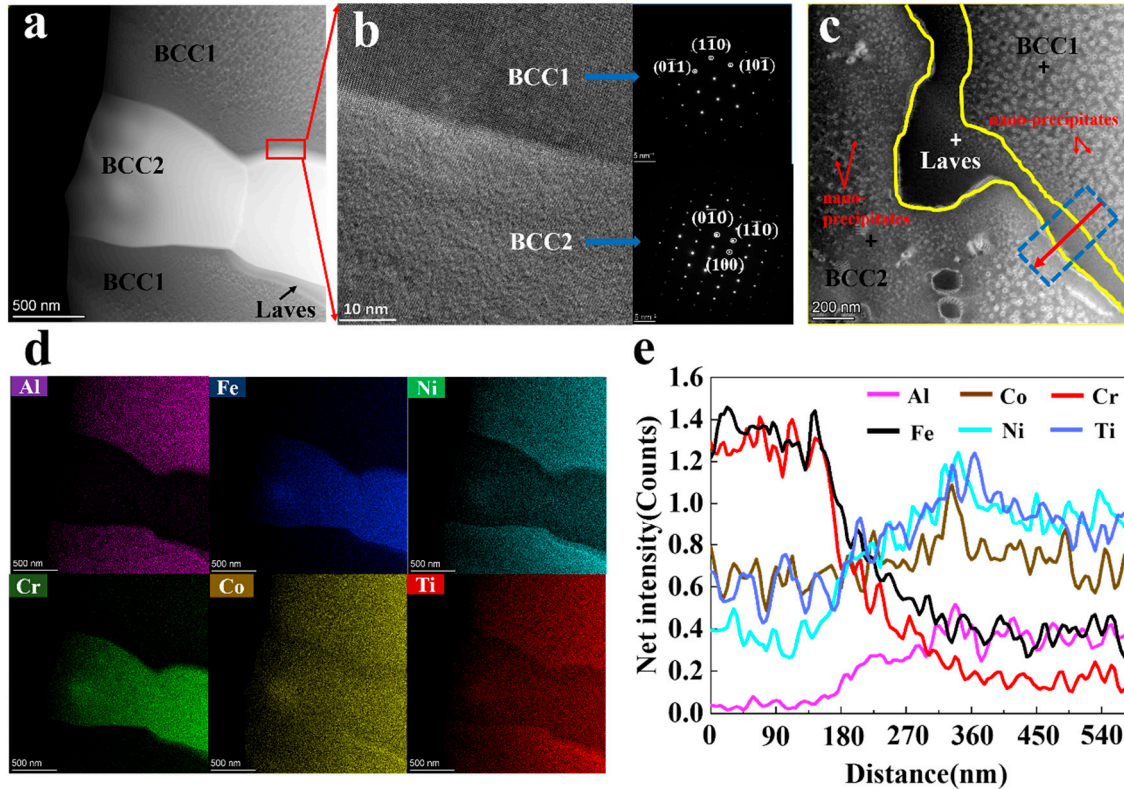

Figure 8. The transmission electron microscope (TEM) images of the $Al_{0.5}$ coating: (**a**) TEM bright-field micrographs; (**b**) High resolution transmission electron microscope (HRTEM) image and Selected area electron diffraction (SAED) of the marked BCC1 and BCC2 phase boundary area in (**a**); (**c**) TEM bright-field magnified micrographs; (**d**) energy dispersive spectrometer (EDS) element mapping of TEM bright imaging in (**a**); and (**e**) selected area line scan image shown by an arrow in (**c**).

Table 5. EDS composition of different points corresponding to the three cross marks in Figure 8c.

Element	Co	Cr	Fe	Ni	Ti	Al
BCC1	20.58	3.99	9.55	25.14	25.58	15.16
BCC2	15.79	28.05	29.94	10.04	14.47	1.71
Laves	18.02	12.80	17.25	20.24	22.01	9.69

In order to further explore the influence of the coating's microstructure change on the performance, the crystal size *D* calculation was performed by the Scherrer equation:

$$D = \frac{k\lambda}{\beta cos\theta} \tag{7}$$

where *D* is mean crystalline size in the nm, *k* is the Scherrer constant, which is usually considered to be 0.89, λ is 0.154056 nm, θ is identified as the position of the diffraction angle of the XRD peak, and β is the Full width at half maximum (FWHM) of the peak at θ (rad). The crystallite size of the Al_0 FCC phase is 36.31 nm. With the increase of the Al element, the crystallite sizes of the BCC1 phase of

$Al_{0.5}$, Al_1 and $Al_{1.5}$ are 39.23 nm, 41.54 nm, and 44.68 nm, and the crystallite size of the BCC2 phase are gradual decline is 34.10 nm, 29.98 nm, and 28.74 nm. The crystallite size of Al_2 coating of a single BCC1 phase is 32.90 nm. It can be found that rapid heating and rapid cooling are the grain refinement of the coating's microstructure, which increases the solubility, produces a lattice distortion effect and a solid solution effect, and improves the hardness and corrosion resistance of the coating. Figure 9 shows the relationship between the phase volume fraction and the average microhardness of the CoCrFeNiTiAl$_x$ HEA alloy coatings. It can be found that the hardness of the alloy is closely related to the addition amount of Al element, and the intrinsic factor is the final phase constitution and microstructure of the alloy. The single-solid solution FCC minimizes the hardness of the Al_0 alloy, due to the fact that the slip system of the FCC structure is much larger than that of the BCC structure. It has been reported that the addition of Al can cause lattice distortion and solid solution effect [22,23]. Referring to the $Al_{0.5}$ HEA coating, the phase transformed from a single FCC into a stable BCC structure, leading to a significantly improved abrasion resistance and hardness of the coating. That is also the reason why only slight adhesive wear occurred during the wear process, which indicates that the BCC2 and Laves phases play a strengthening role in the alloy. When the addition of Al increased, solid solution saturation occurred and a low hardness phase of BCC1 became the majority. However, the Al_2 coating experienced large flaky flaking in the wear resistance experiment, possessing a micro-fracture (peeling) wear mechanism, which may be attributed to the brittleness of the BCC1 phase, the result is consistent with the required change in crystallite size. This also confirms the results of previous studies, because laser cladding has a higher cooling rate, the higher solidification rate is beneficial to the formation of BCC phase and improves the hardness.

The corrosion test proves that the addition of Al also has a significant effect on the corrosion resistance of the CoCrFeNiTiAl$_x$ HEA alloy coatings. Using the Al_0 coating with a single FCC structure containing a large amount of Cr and Ti elements, it is easy to form Cr_2O_3, TiO_2, and Ti_2O_3 passivation films, which enhances the corrosion resistance of the coating. As a passive element, the addition of a small amount of Al will form an Al_2O_3 passivation film, which can further improve the corrosion resistance of the $Al_{0.5}$ coating. With the increase of Al content to one or higher, the structure of the coating changed significantly. The dendrite content gradually increased and the interdendritic content decreased. Consequently, the increased grain boundaries exhibiting a higher dislocation density and corrosion activity made them more susceptible to corrosion by the medium. Furthermore, the secondary precipitation effect produced by the higher content accelerated the pitting corrosion of Al in the coating. Thus, the Al_2 coating shows the lowest corrosion resistance among the five coatings. At the same time, according to the previous calculation of the crystallite size, it can be proved that when x = 0.5, the crystallite size difference between the BCC1 and BCC2 phases is the smallest, so its corrosion resistance performance is the best.
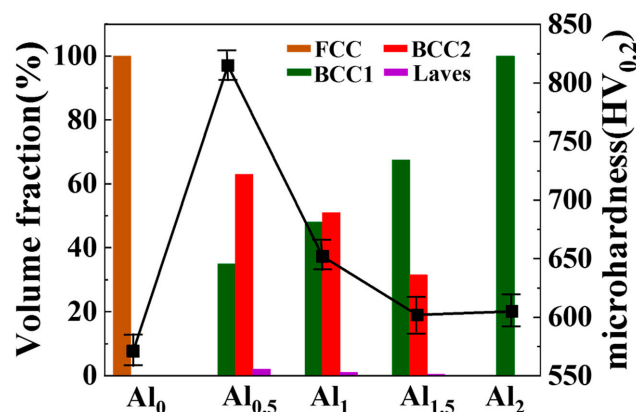

Figure 9. Relationship between the volume fraction of the phases and the average microhardness of the coatings.

Figure 10 shows the comparison of the self-corrosion potential E_{corr} and the self-corrosion current density I_{corr} of the six HEAs: CoCrFeNiTiAl$_x$, CoCrFeNi, Al$_x$CoCrFeNi, Al$_x$CoCrFeMnNi, CoCrFeNiAiTi$_x$, and Al$_x$CoCrFe$_{2.7}$NiMo [6,12,26,27]. The introduction of Ti element can promote the passivation behavior of the coating due to the formation of TiO$_2$ and Ti$_2$O$_3$ phases. Adding Mo to the CoCrFeNiAl alloy can result in a significant improvement in the corrosion resistance of the alloy, which is ascribed to the fact that Mo can easily produce a dense passivation film. It is generally believed that Al$_2$O$_3$ with a dense structure can effectively resist Cl$^-$ ion corrosion. While a further increase in Al content leads to an increase in the volume fraction of (Ni,Al)-rich BCC1 phases, which is susceptible to Cl$^-$ ion corrosion and reduces the local corrosion resistance of the passivation film. Based on this study, the reason for the decrease in corrosion resistance may be attributed to the microstructure evolution. In addition, the changed metal oxide content in the passivation film may play a certain role. Consequently, there should be an interaction between the passivation behavior and the effect of the metal oxide content on the corrosion resistance of HEA alloys and coatings.
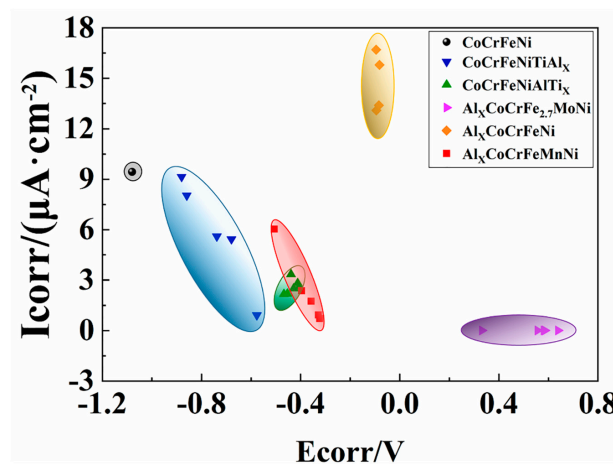

Figure 10. Comparison of the corrosion resistance of CoCrFeNi, Al$_x$CoCrFeNi, CoCrFeNiAlTi$_x$, Al$_x$CoCrFeMnNi, Al$_x$CoCrFe$_{2.7}$MoNi, and CoCrFeNiTiAl$_x$ HEAs in a 3.5 wt.% NaCl solution.

4. Conclusion

In this work, the CoCrFeNiTiAl$_x$ (x = 0, 0.5, 1, 1.5, 2) coatings were prepared on the surface of AISI1045 steel by laser cladding technology, and its microstructure, hardness, wear resistance, and corrosion resistance were analyzed.

- Under the conditions of high laser power and fast solidification rate, the increase in Al content promoted the transition from a single FCC phase to the BCC1 and BCC2 phases, and a small amount of Laves phase. Due to the larger atomic radius of Al, as the Al element increases, the lattice distortion energy increases, and the BCC2 phase gradually decreases to form a relatively stable BCC1 phase.
- As the Al content increases, the hardness and abrasion resistance of the coating first increase and then decrease. The crystallite size of each phase of the coating also changed, and the grains gradually refined. The grain size difference between the two phases of the Al$_{0.5}$ coating was the smallest. The grain refinement resulted in the highest hardness of the Al$_{0.5}$ coating, reaching 880 HV, 6.5 times that of the substrate. The abrasion mechanism was the transition from abrasive wear to slight adhesive wear, and finally to micro-fracture (flake) wear.
- The corrosion resistance of the CoCrFeNiTiAl$_x$ HEA coatings in a 3.5% NaCl solution increased first, then decreased with increasing Al content. The addition of a small amount of Al will form an Al$_2$O$_3$ passivation film, the self-corrosion potential of Al$_{0.5}$ was the most positive, at -0.5766 V, while the self-corrosion current density was the smallest, at 9.13×10^{-7} A·cm^{-2}. The Al$_{0.5}$ coating

showed good corrosion resistance. This also proves that when there are multiple phases, the performance of the alloy may be better when the crystallite size difference of each phase is small.

- The results show that adding a small amount of aluminum can refine the grains of the CoCrFeNiTiAl$_x$ coating and improve the corrosion resistance and mechanical properties of the coating. CoCrFeNiTiAl$_{0.5}$ exhibits the best performance among the as-prepared coatings, can significantly improve the surface properties of AISI1045 steel.

Author Contributions: General program development and writing, Y.X.; Experiment, Z.L. and J.L.; Experiment guide, F.Z. and L.W.; Compress test, J.H.; Microstructure analysis guide, Y.C.; Theory guide, L.L. All authors have read and agreed to the published version of the manuscript.

Conflicts of Interest: The authors declare no conflicts of interest.

References

1. Yeh, J.W.; Chen, S.K.; Lin, S.J.; Gan, J.Y.; Chin, T.S.; Shun, T.T.; Tsau, C.H.; Chang, S.Y. Nanostructured high-entropy alloys with multiple principal elements: Novel alloy design concepts and outcomes. *Adv. Eng. Mater.* **2004**, *6*, 299–303. [CrossRef]
2. Zhang, Y.; Zuo, T.T.; Tang, Z.; Gao, M.C.; Dahmen, K.A.; Liaw, P.K.; Lu, Z.P. Microstructures and properties of high-entropy alloys. *Prog. Mater. Sci.* **2014**, *61*, 1–93. [CrossRef]
3. Zhang, Y.; Zhou, Y.J.; Lin, J.P.; Chen, G.L.; Liaw, P.K.; Zhang, Y. Solid-solution phase formation rules for multi-component alloys. *Adv. Eng. Mater.* **2008**, *10*, 534–538. [CrossRef]
4. Li, C.; Li, J.C.; Zhao, M.; Zhao, M.; Jiang, Q. Effect of alloying elements on microstructure and properties of multiprincipal elements high-entropy alloys. *J. Alloys Compd.* **2009**, *475*, 752–757. [CrossRef]
5. Chuang, M.H.; Tsai, M.H.; Wang, W.R.; Lin, S.J.; Yeh, J.W. Microstructure and wear behavior of Al$_x$Co$_{1.5}$CrFeNi$_{1.5}$Ti$_y$ high-entropy alloys. *Acta Mater.* **2011**, *59*, 6308–6317. [CrossRef]
6. Shang, C.; Axinte, E.; Ge, W.; Zhang, Z.; Wang, Y. High-entropy alloy coatings with excellent mechanical, corrosion resistance and magnetic properties prepared by mechanical alloying and hot pressing sintering. *Surf. Interfaces* **2017**, *9*, 36–43. [CrossRef]
7. Chew, Y.; Bi, G.J.; Zhu, Z.G.; Ng, F.L.; Weng, F.; Liu, S.B.; Nai, S.M.L.; Lee, B.Y. Microstructure and enhanced strength of laser aided additive manufactured CoCrFeNiMn high entropy alloy. *Mater. Sci. Eng. A* **2019**, *744*, 137–144. [CrossRef]
8. Liu, G.; Liu, L.; Liu, X.; Wang, Z.; Han, Z.; Zhang, G.; Kostka, A. Microstructure and mechanical properties of Al$_{0.7}$CoCrFeNi high-entropy-alloy prepared by directional solidification. *Intermetallics* **2018**, *93*, 93–100. [CrossRef]
9. Hong, S.; Wu, Y.; Li, G.; Wang, B.; Gao, W.; Ying, G. Microstructural characteristics of high-velocity oxygen-fuel (HVOF) sprayed nickel-based alloy coating. *J. Alloys Compd.* **2013**, *581*, 398–403. [CrossRef]
10. Wang, C.; Yu, J.; Zhang, Y.; Yu, Y. Phase evolution and solidification cracking sensibility in laser remelting treatment of the plasma-sprayed CrMnFeCoNi high entropy alloy coating. *Mater. Des.* **2019**, *182*, 108040. [CrossRef]
11. Anupam, A.; Kottada, R.S.; Kashyap, S.; Meghwal, A.; Murty, B.; Berndt, C.; Ang, A. Understanding the microstructural evolution of high entropy alloy coatings manufactured by atmospheric plasma spray processing. *Appl. Surf. Sci.* **2019**, *505*, 144117. [CrossRef]
12. Liu, J.; Liu, H.; Chen, P.; Hao, J. Microstructural characterization and corrosion behaviour of AlCoCrFeNiTi$_x$ high-entropy alloy coatings fabricated by laser cladding. *Surf. Coat. Technol.* **2019**, *361*, 63–74. [CrossRef]
13. Zhang, S.; Wu, C.L.; Zhang, C.H.; Guan, M.; Tan, J.Z. Laser surface alloying of FeCoCrAlNi high-entropy alloy on 304 stainless steel to enhance corrosion and cavitation erosion resistance. *Opt. Laser Technol.* **2016**, *84*, 23–31. [CrossRef]

14. Matilainen, V.; Piili, H.; Salminen, A.; Syvänen, T.; Nyrhilä, O. Characterization of process efficiency improvement in laser additive manufacturing. *Phys. Procedia* **2014**, *56*, 317–326. [CrossRef]

15. Ocelík, V.; Janssen, N.; Smith, S.N.; De Hosson, J.T.M. Additive Manufacturing of High-Entropy Alloys by Laser Processing. *JOM* **2016**, *68*, 1810–1818. [CrossRef]

16. Liu, Y.Y.; Chen, Z.; Chen, Y.Z.; Shi, J.C.; Wang, Z.Y.; Wang, S.; Liu, F. Effect of Al content on high temperature oxidation resistance of Al$_x$CoCrCuFeNi high entropy alloys (x = 0, 0.5, 1, 1.5, 2). *Vacuum* **2019**, *169*, 108837. [CrossRef]

17. Zhang, K.; Fu, Z. Effects of annealing treatment on phase composition and microstructure of CoCrFeNiTiAl$_x$ high-entropy alloys. *Intermetallics* **2012**, *22*, 24–32. [CrossRef]

18. Liu, Y.Y.; Chen, Z.; Chen, Y.; Shi, J.; Wang, Z.; Zhang, J. The effect of Al content on microstructures and comprehensive properties in Al$_x$CoCrCuFeNi high entropy alloys. *Vacuum* **2019**, *161*, 143–149. [CrossRef]

19. Jiang, S.; Lin, Z.; Xu, H.; Sun, Y. Studies on the microstructure and properties of Al$_x$CoCrFeNiTi$_{1-x}$ high entropy alloys. *J. Alloys Compd.* **2018**, *741*, 826–833. [CrossRef]

20. Kao, Y.F.; Lee, T.D.; Chen, S.K.; Chang, Y.S. Electrochemical passive properties of Al$_x$CoCrFeNi (x = 0, 0.25, 0.50, 1.00) alloys in sulfuric acids. *Corros. Sci.* **2010**, *52*, 1026–1034. [CrossRef]

21. Guo, S.; Liu, C.T. Phase stability in high entropy alloys: Formation of solid-solution phase or amorphous phase. *Prog. Nat. Sci. Mater. Int.* **2011**, *21*, 433–446. [CrossRef]

22. Archard, J.F. Contact and Rubbing of Flat Surfaces. *J. Appl. Phys.* **1953**, *24*, 981–988. [CrossRef]

23. Zhou, Y.J.; Zhang, Y.; Wang, F.J.; Chen, G.L. Phase transformation induced by lattice distortion in multiprincipal component CoCrFeNiCu$_X$Al$_{1-x}$ solid-solution alloys. *Appl. Physics. Lett.* **2008**, *92*, 121–123. [CrossRef]

24. Courtney, T. *Mechanical Behavior of Materials*; McGraw-Hill: New York, NY, USA, 1990; p. 173.

25. Tong, C.J.; Chen, M.R.; Yeh, J.W.; Lin, S.J.; Chen, S.K.; Shun, T.T.; Chang, S.Y. Mechanical performance of the Al$_x$CoCrCuFeNi high-entropy alloy system with multiprincipal elements. *Metall. Mater. Trans. A* **2005**, *36*, 1263–1271. [CrossRef]

26. Sha, M.; Jia, C.; Qiao, J.; Feng, W.; Ai, X.; Jing, Y.-A.; Shen, M.; Li, S. Microstructure and Properties of High-Entropy Al$_x$CoCrFe$_{2.7}$MoNi Alloy Coatings Prepared by Laser Cladding. *Metals* **2019**, *9*, 1243. [CrossRef]

27. Ye, F.; Jiao, Z.; Yan, S.; Guo, L.; Feng, L.; Yu, J. Microbeam plasma arc remanufacturing: Effects of Al on microstructure, wear resistance, corrosion resistance and high temperature oxidation resistance of Al$_x$CoCrFeMnNi high-entropy alloy cladding layer. *Vacuum* **2020**, *174*, 109178. [CrossRef]